Weyl semimetal in the rare-earth hexaboride family supporting a pseudonodal surface and a giant anomalous Hall effect

Ruiqi Zhang, Cheng-Yi Huang, Jamin Kidd, Robert S. Markiewicz, Hsin Lin, Arun Bansil, Bahadur Singh, and Jianwei Sun

Phys. Rev. B **105**, 165140 — Published 21 April 2022

DOI: 10.1103/PhysRevB.105.165140

A Weyl Semimetal in the Rare-Earth Hexaboride Family Supporting a Pseudo-Nodal surface and a Giant Anomalous Hall Effect

Ruiqi Zhang,[1,*] Cheng-Yi Huang,[2,*] Jamin Kidd,[1] Robert S. Markiewicz,[2]
Hsin Lin,[3] Arun Bansil,[2] Bahadur Singh,[4,†] and Jianwei Sun[1,‡]

[1]*Department of Physics and Engineering Physics, Tulane University, New Orleans, LA 70118, USA*
[2]*Department of Physics, Northeastern University, Boston, MA 02115, USA*
[3]*Institute of Physics, Academia Sinica, Taipei 11529, Taiwan*
[4]*Department of Condensed Matter Physics and Materials Science, Tata Institute of Fundamental Research, Mumbai 400005, India*

Rare-earth hexaborides offer a rich tapestry for exploring the interplay of topological orders, magnetism, and electron-correlation effects associated with protected quantum phenomena. Here, using first-principles modeling, we identify in cerium hexaboride (CeB_6) a new topological state that harbors a pseudo-nodal surface (PNS) along with double-Weyl fermions. An analysis of the electronic states in the vicinity of the Fermi level reveals the presence of M_z-mirror-symmetry-protected band crossings that involve itinerant (d) and localized (f) states of Ce. These band crossings are found to remain nearly gapless as one goes away from the mirror plane, driving the formation of PNS states. We also demonstrate the presence of coexisting double-Weyl fermions with chiral charges of ± 2 on the C_{4z} rotational axis. By analyzing the Berry curvature field associated with the topological states, we predict that CeB_6 supports a giant anomalous Hall conductivity of -1840 Ω^{-1}cm^{-1} in the slightly electron-doped regime, which would be larger than the values reported to date in magnetic Weyl semimetals. Our study thus indicates that CeB_6, which combines ferromagnetic order with topological physics in a heavy-fermion matrix, would provide a promising new playground for investigating topological magnetic states with giant anomalous Hall responses.

Introduction. Rare-earths provide exciting opportunities for realizing emergent correlated states that include heavy fermions, unconventional superconductivity, quantum critical fluctuations, non-Fermi liquids, and multipolar phases [1–3]. The appearance of these novel states is driven by the many-body interactions between the local spins of rare-earth ions and the conduction electrons at low temperatures. Correlated topological states have also been proposed in the rare-earth family [4–7]. Prominent examples include SmB_6 (topological Kondo insulator (TKI)) [8–10], CeNiSn (Mobius-Kondo insulator) [11], CeAlSi and PrAlSi (magnetic Weyl semimetals) [12–14], and $Ce_3Bi_4Pd_3$ (Weyl-Kondo semimetal) [6, 7]. Experimental realization, however, remains limited to the observation of the TKI state in SmB_6 [10, 15] and the magnetic Weyl semimetal states in CeAlSi [12] and PrAlSi [14, 16]. The rare-earth hexaboride family has also been actively used to search for topological magnetic phases, e.g. EuB_6 [17, 18].

There is great need to discover new correlated topological materials for fundamental science studies as well as for the next-generation device applications. Here, the rare-earth hexaborides present an attractive materials family since it is well-known to provide a rich tapestry of electronic ground states [10]. CeB_6 is particularly interesting because it exhibits an intricate magnetic phase diagram that includes a hidden antiferromagnetic quadrupolar phase [19–22]. The complex magnetic structure of CeB_6 is driven by the unique spin and orbital orderings resulting from electron correlation effects. So motivated, we explore the topological structure of the ferromagnetic (FM) phase of CeB_6 using an accurate parameter-free, first-principles modeling framework. We find that CeB_6 hosts a coexisting pseudo-nodal surface (PNS) with a nodal-surface with a small gap of <5meV along with double-Weyl fermions that lie close to the Fermi level. By investigating the Berry curvature associated with topological crossings, we predict that CeB_6 supports a large anomalous Hall conductivity (AHC), which is larger than the values reported to date in magnetic materials [23]. We also discuss topological surface states and their thickness-dependent anomalous Hall response in CeB_6.

Topological semimetals can be broadly classified in terms of the dimensionality of their band crossings as zero-dimensional (0D) nodal-point, one-dimensional (1D) nodal-line, and two-dimensional (2D) nodal-surface semimetals [24–28]. Nodal-point semimetals can be further subdivided into single or multi-Weyl fermion, Dirac, or higher-fold fermion semimetals depending on the band degeneracy at the crossing point and the symmetries involved [29–32]. The nodal-point crossings can be preserved in the presence of planar symmetries to realize 1D Dirac or Weyl nodal lines or 2D nodal surface crossings. While the Weyl nodal-line states have been reported in recent experiments on Co_2MnGa [33], the realization of 2D nodal surface fermions has remained challenging.

CeB_6 crystallizes in $Pm\bar{3}m$ (No. 221) space group which contains various rotational and mirror-symmetries. Three distinct low-temperature magnetic states have been identified in CeB_6: an antiferromagnetic phase below $T_N = 2.3\ K$, an antiferromagnetic (AFM) quadrupolar phase between $T_N = 2.4\ K$ to $T_Q = 3.4$ K, and a para-

magnetic phase above 3.4 K [19, 20]. However, the most recent inelastic neutron-scattering experiments indicate the presence of a low-energy FM state [34] and point to the importance of competing magnetic orders in the material. We will focus on the FM state of CeB_6 that breaks time-reversal symmetry and makes all the electronic bands in the system essentially singly degenerate. When combined with the mirror and rotational symmetries, these singly degenerate bands with opposite mirror or rotational eigenvalues cross to realize PNS and double-Weyl fermions as shown schematically in Fig. 1(a)-(c).

Methods. Electronic structure calculations were performed using the Vienna ab-initio simulation package (VASP) [35, 36] based on the projector-augmented wave method [37]. A high-energy cutoff of 520 eV was used to truncate the plane-wave basis set. The exchange-correlation effects were treated using the strongly-constrained-and appropriately-normed (SCAN) meta-GGA functional [38]. The charge, spin and lattice degrees of freedom were all treated on an equal footing in the computations without invoking any free parameters such as the Hubbard U. Previous studies works have shown the efficacy of SCAN for accurately modeling ground states and electronic structure of strongly correlated systems such as the cuprates [39–41] and nickelates [42], binary 3d oxides [43], and especially the f-electron system SmB_6 [8], due to the reduction of self-interaction error in comparison with other widely used density functionals [43]. We adopted a $16 \times 16 \times 16$ Γ-centered k mesh to sample the primitive bulk BZ and total energy calculations. SOC effects were included self-consistently. The crystal structures and ionic positions were fully optimized with a force convergence criterion of 0.001 eV/Å for each atom and a total energy tolerance of 10^{-6} eV. Our optimized structural parameters, revealing an FM ground state, were used for electronic structure calculations. Topological properties were calculated by using a material-specific, effective tight-binding model Hamiltonian generated using the VASP2WANNIER90 [44] interface. Ce d and f and B p orbitals were included in constructing the Wannier functions. The surface spectral weight of semi-infinite slabs was calculated using an iterative Green's function method [45, 46].

Crystal and electronic structures. The crystal structure of the nonmagnetic state of CeB_6 is presented in Fig. 1(d). It is a CsCl-type structure where Ce atoms lie at the corners and the B_6 octahedral clusters are located at the body centers of the cubic lattice. The system preserves 48 symmetry operations of the cubic lattice including the mirror-planes, rotational axis, and inversion symmetries. For the FM order with Ce spins aligned parallel to the (001) direction [Fig. 1(e)], symmetry of the system is lowered to contain one mirror plane M_z, a four-fold rotational axis C_{4z}, and the inversion symmetry. The breaking of the time-reversal symmetry ensures that all bands are singly degenerate. The optimized lattice parameter a is found to be 4.110 Å, which is in good agreement with the corresponding experimental value [47]. The calculated magnetic moment of Ce ions is $\sim$1.0 μ_B, which is consistent with our Ce $4f$ occupation in calculations including spin-orbit coupling (SOC). The bulk and (001)-surface BZs are shown in Fig. 1(f).

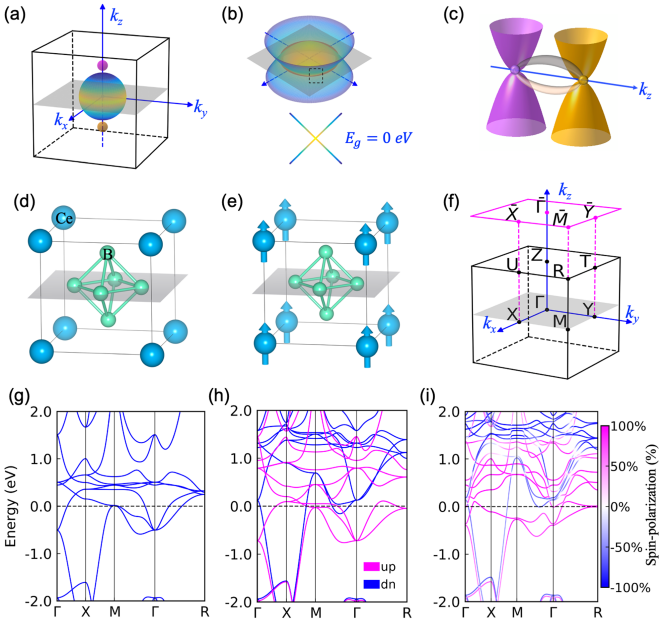

FIG. 1. Topological state, crystal structure and band structure of CeB_6. (a)-(c) Coexisting PNS and double-Weyl fermions. The nodal crossings that form the nodal surface are protected on the $M_z = 0$ mirror plane marked with shaded gray. These nodal crossings interact weakly away from the M_z mirror-plane, remaining nearly degenerate to form a PNS. (c) A pair of double-Weyl fermions with chiral charge $C_w = \pm 2$ on the C_{4z} rotational axis with double Fermi arc surface states. Crystal structure of (d) nonmagnetic and (e) ferromagnetic CeB_6. Blue and green balls represent Ce and B atoms, respectively. (f) Primitive bulk Brillouin zone (BZ) of CeB_6 with relevant high-symmetry points. The projected plane represents the associated (001) surface BZ and the dashed lines locate the projection of bulk high-symmetry points on the (001) surface. First-principles band structure of (g) nonmagnetic and (h) ferromagnetic CeB_6. (i) Spin-resolved electronic structure of ferromagnetic CeB_6 with spin-orbit coupling (SOC). Color scale gives the spin-polarization of the states.

We have carried out computations on CeB_6 with symmetry-lowered structures, see Supplementary Table S1 [48], and found several low-energy magnetic phases which lie within 5 meV/atom of the ground state, indicating the presence of many magnetic states that are nearly degenerate with the ground state. This result is similar to the findings in recent studies of other correlated compounds, such as the cuprates and SmB_6, where many magnetic states have been found to compete at low temperatures [8, 39, 42, 43, 49]. We note that many ex-

perimental studies report finding strong magnetic fluctuations at low temperatures in CeB_6, suggesting that the ground state of CeB_6 involves competing orders and that it is not homogeneous. These experimental results are in good accord with our theoretical results given in the Supplementary Table S1 and support the notion that CeB_6 is a strongly correlated metal. Interestingly, a ferromagnetic/antiferromagnetic crossover has been reported in the magnetic phase diagram of CeB_6 [50], so that our predicted ferromagnetic state with novel topological features should be amenable to experimental realization.

Figure 1(g) shows the calculated band structure of nonmagnetic CeB_6 in the absence of SOC. It can be seen that valence and conduction bands dip into each other, forming a connected band-crossing structure in the vicinity of the Fermi level. The bands are seen to cross along the $\Gamma - X$ line and maintain multiple degeneracies at the Γ and M points. These band crossings primarily consist of itinerant d and localized f orbitals of Ce. Upon considering the calculated ferromagnetic order, the bands form two spin-split channels. The spin-splitting is strongly dependent on momentum (k) and reaches as large as $\sim$1 eV at the Γ point, indicating a complex exchange-coupling behavior in agreement with experiments [19, 34]. The band crossings evolve from the nonmagnetic structure with additional band crossings forming between up and down spin states along the $\Gamma - X$ and $X - M$ directions [Fig.1(h)]. Figure 1(i) shows the FM band structure with SOC. Although band structure changes due to strong SOC effects, the band crossings along $\Gamma - X$ and $X - M$ are preserved.

We emphasize that FM band structure with SOC clearly shows flat bands associated with Ce-f orbitals with small dispersion (-0.20 eV) along the $X - M$ direction and hole bands along $\Gamma - R$. There is an additional band inversion between Ce d and B p states deep in the valence region around -2.0 eV at X. These features agree with earlier DFT+U [51] and DMFT calculations [52] and reproduce the ARPES experiments in greater detail [53, 54].

Pseudo-nodal surfaces and double-Weyl nodes. We now consider the topological properties of FM CeB_6. To locate the nodal band crossings in the full BZ, we constructed an effective tight-binding model Hamiltonian informed by our first-principles computations, see Methods section for details. Figures 2(a) and (b) show M_z mirror-eigenvalue-resolved band structure on $k_z = 0$ and $k_z = \pi/a$ planes, respectively. There are clear band crossings between the opposite-mirror-eigenvalue states on both planes. A planar rendition of these band crossings resolves mirror-symmetry-protected nodal lines on $k_z = 0$ and $k_z = \pi/a$ planes [Figs. 2(c) and (d)]. Interestingly, upon scanning the band crossings in the full 3D BZ, these nodal-line crossings are weakly hybridized away from the mirror planes. They realize two PNSs. The closed nodal surface shown in Fig. 2 (e) forms around the $k_z = 0$ plane and an open nodal surface appears around the $k_z = \pi/a$ planes [Fig. 2 (f)].

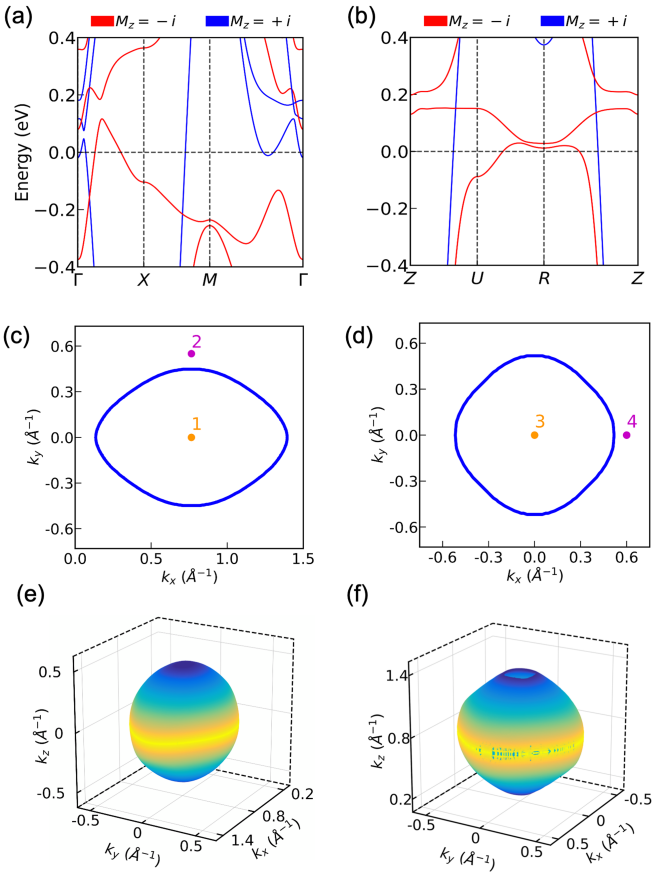

FIG. 2. Pseudo-nodal-surface in CeB_6. M_z mirror-eigenvalue-resolved band structures of CeB_6 (including SOC) at (a) $k_z = 0$ and (b) $k_z = \pi/c$ planes. Red and blue curves identify bands with $+i$ and $-i$ M_z mirror-eigenvalues. These bands form protected crossings on the mirror-planes. (c)-(d) Nodal band-crossings on (c) $k_z = 0$ and (d) $k_z = \pi/a$ planes. Numbers 1, 2, 3, and 4 on graphs identify inner and outer regions of the nodal lines (see text for details). (e)-(f) Distribution of nodal band-crossings in the bulk BZ. The band crossings form a (e) a closed nodal surface surrounding the $k_z = 0$ plane and (f) open nodal surface around $k_z = \pi/a$ plane. Color scales represent the k_z value of the nodal band crossings.

Since M_z is preserved in (001) FM CeB_6, the states on the $k_z = 0$ and π mirror-invariant planes can be labeled by $\pm i$ mirror eigenvalues. To determine the number of band inversions and topological protection of these states, we first focus on the crossing points on the mirror-invariant planes and define the index $N_{k_1\,k_2}$:

$$N_{k_1 k_2} = N_{k_1} - N_{k_2},$$

where N_k is the number of occupied states with $+i$ mirror eigenvalue at the k point. Interestingly, both N_{12} and N_{34} takes a value of 1 in both Figs. 2(c) and (d), respectively, which implies that a single band inversion

happens as one goes from the inner side to the outer side of the nodal line. Thus, the band crossings on the mirror-invariant plane are symmetry protected. However, the band crossings away from the mirror-invariant plane are not symmetry-protected. They display a negligible gap as the interaction among the crossing bands is small, realizing PNS crossings [55]. We have further checked their robustness by artificially varying the SOC strength in our computations, see Supplemental Materials (SM) [48]. The pseudo-nodal crossings stay robust even when the SOC strength is increased by 500%. Such nodal crossings can enhance Berry curvature effects and lead to large anomalous Hall responses.

Concerning the stability of the nodal surfaces, we emphasize first that nodal surface crossings are generally protected by global symmetries such as the antiunitary PC symmetry, where P and C denote the inversion and particle-hole symmetry, respectively [55, 56]. However, such symmetries have been difficult to realize in materials with strong spin-orbit coupling effects. Notably, planar symmetries involving mirror-planes can also protect the nodal crossings that lie on these planes. If the coupling between the crossing bands is weak, as we find here to be the case in CeB_6 and in the systems reported in Ref. [55], the PNSs are realized. Backbone of the PNS is formed by the mirror-protected nodal lines and a vanishing gap between the crossing bands away from the nodal lines is maintained by the weak interactions, see Ref. [55].

Besides the PNS crossings, the bands in the vicinity of the Fermi level cross to form robust single and double Weyl fermions. Figure 3(a) illustrates the 18 Weyl nodes in CeB_6 whose coordinates are listed in Table S1 of SM [48]. There are 16 single and 2 double-Weyl nodes lying across the $k_z = 0$ plane in the whole BZ. Interestingly, a pair of single and double-Weyl nodes are located on the C_{4z} rotational axis which can be characterized based on C_{4z} rotational eigenvalues [57]. Notably, C_{4z} rotational symmetry can protect Weyl nodes of both charge 1 or 2 that appear as crossing points between the different rotational eigenvalues. We define the ratio u_c/u_v, where u_c (u_v) is the C_{4z} rotational eigenvalue of the conduction (valence) band at the Weyl nodes, to determine the chiral charge of the Weyl nodes. The chiral charge of Weyl nodes should be ±1 (±2) when $u_c/u_v = \pm i$ (-1). Figure 3(b) shows C_{4z} eigenvalue-resolved band structure where both chiral charge C_w of ±1 and ±2 Weyl nodes are seen. The associated Berry curvature on the $k_x = 0$ plane is shown in Figs. 3(c) and (d) where the Weyl nodes are seen as source and sink of the Berry curvature field. To showcase the nontrivial surface states appearing due to the important bulk-boundary correspondence, we investigate the surface states on both (001) and (100) surfaces, see SM. However, we find that the nontrivial surface states are masked by the projected bulk bands and may not be distinctly resolved in experiments.

Anomalous Hall conductivity. Having established PNS and Weyl nodal crossings in CeB_6, we now address the expected anomalous Hall response from such nontrivial states. In this connection, we calculate anomalous Hall conductivity (AHC) σ_{xy} using

$$\sigma_{xy} = \frac{e^2}{\hbar}\int \frac{d^3k}{(2\pi)^3}\Omega^z_{xy}(\boldsymbol{k}) \tag{1}$$

where the Berry curvature is defined as

$$\Omega^z_{xy}(\boldsymbol{k}) = -2\mathrm{Im}\sum_{n\in\mathrm{occ.}}\sum_{m}\frac{\left\langle n\left|\frac{\partial H(\boldsymbol{k})}{\partial k_x}\right|m\right\rangle\left\langle m\left|\frac{\partial H(\boldsymbol{k})}{\partial k_y}\right|n\right\rangle}{(E_n - E_m)^2} \tag{2}$$

In Eq. 2, $|n\rangle$ denotes the n^{th} state counted from the lowest occupied valence band [58]. Figure 4(a) shows the calculated AHC σ_{xy} as a function of energy. σ_{xy} shows a value of -627 $\Omega^{-1}\mathrm{cm}^{-1}$ at the fermi level and reaches a maximum value of -1840 $\Omega^{-1}\mathrm{cm}^{-1}$ near 0.15 eV compared to 1100 $\Omega^{-1}\mathrm{cm}^{-1}$ in $Co_3Sn_2S_2$ [23]. The large AHC could thus be accessed in electron-doped CeB_6. To the best of our knowledge, such a large AHC has not been observed before. We present the calculated Berry

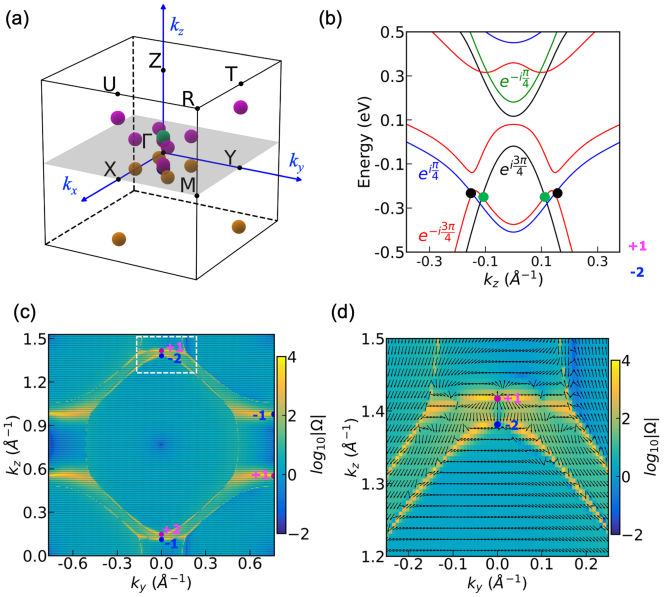

FIG. 3. Weyl nodes and Berry curvature field in CeB_6. (a) $k-$space location of the Weyl nodes in 3D bulk Brillouin zone. Pink (yellow) balls represent the Weyl points of chiral charge $+1$ (-1), while green (blue) balls represent the Weyl points of chiral charge $+2$ (-2). (b) C_{4z} rotational eigenvalue resolved band structure of CeB_6 on the k_z axis. $e^{i(3\pi/4)}$, $e^{i(\pi/4)}$, $e^{-i(\pi/4)}$, and $e^{-i(3\pi/4)}$ denote C_{4z} eigenvalue of the bands. Black (green) dots denote the chiral charge $C_w = 2(1)$ of the Weyl nodes. (c) The distribution of Berry curvature on $k_x = 0$ plane. Pink and blue dots denote the Weyl points with positive and negative chiral charge, respectively. (d) Closeup of the area highlighted in (c). Colorbar denotes the magnitude of Berry curvature on a logarithmic scale and arrows represent the Berry curvature field.

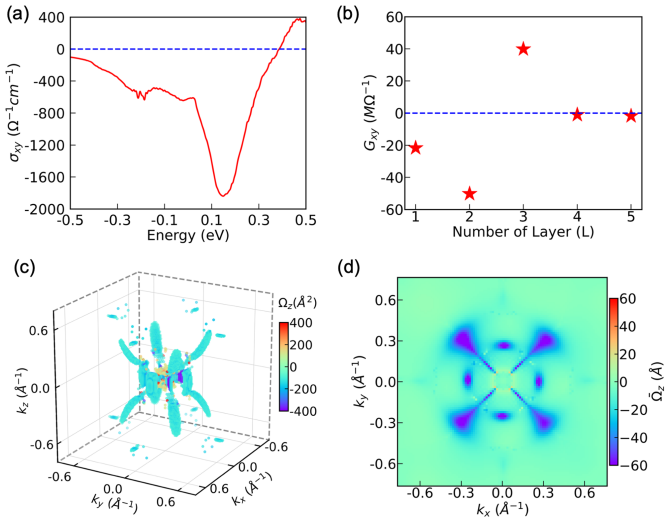

FIG. 4. Calculated anomalous Hall conductivity of bulk and thin-film of CeB_6. (a) Energy dependence of anomalous Hall σ_{xy} on the (001) plane of CeB_6. (b) Berry curvature ($\Omega^z_{xy}(\boldsymbol{k})$) distribution in the 3D $k_x-k_y-k_z$ space. (c) The accumulated Berry curvature along the k_z direction. (d) 2D anomalous Hall conductance G_{xy} as a function of CeB_6 layers (L).

curvature in Fig. 4(b) and the accumulated Berry curvature along k_z in Fig. 4(c). The dominant Berry curvature hotspots are visible along the $k_x = \pm k_y$ planes. This is apparent since both the vertical mirror symmetries normal to [110] and [1$\bar{1}$0] directions are broken in the presence of the SOC. This symmetry breaking leads to an inverted bandgap as large as 80 meV at the nodal band crossings.

To showcase finite-size effects on the anomalous Hall response in engineered thin films of CeB_6, we present calculated anomalous Hall conductance G_{xy} as a function of layer-thickness L in Fig. 4(d). G_{xy} is -50.23 MΩ^{-1} as $L/a = 2$ corresponding to the anomalous Hall conductivity $G_{xy}/L = -611\ \Omega^{-1}\text{cm}^{-1}$. These results suggest that CeB_6 will show anomalous Hall response in both bulk and in the engineered thin films.

In summary, we have delineated in-depth the topological electronic structure and the associated anomalous Hall response in the FM state of CeB_6. Based on parameter-free, first-principles modeling, we unveil the presence of both the PNS fermions and Weyl fermions in CeB_6. These correlated topological states are formed through interactions between the itinerant (d) and localized (f) orbitals of Ce. Our analysis reveals that M_z mirror-symmetry-protected band crossings in the vicinity of the Fermi level yield PNS fermions with coexisting double-Weyl fermions with chiral charge ± 2 on the C_{4z} rotational axis. The computed AHC associated with the topological states in CeB_6 is found to be larger than the values that have been reported to date in currently known magnetic materials. Our study thus indicates that CeB_6 is a highly promising material for exploring correlated topological phenomena in a heavy-fermion matrix for fundamental science studies as well as for future device applications.

Acknowledgments. The work at Tulane University was supported by the U.S. DOE, Office of Science, Basic Energy Sciences Grant No. DE-SC0014208, the American Chemical Society Petroleum Research Fund PRF number:59480-DNI5, the Cypress Computational Cluster at Tulane, the Extreme Science and Engineering Discovery Environment (XSEDE), and the National Energy Research Scientific Computing Center. The work at Northeastern University was supported by the Air Force Office of Scientific Research under award number FA9550-20-1-0322 (Weyl materials discovery for optoelectronics applications), and it benefited from the computational resources of Northeastern University's Advanced Scientific Computation Center (ASCC) and the Discovery Cluster. Additional support was provided by DOE Office of Basic Energy Sciences Program E3B5. The work at TIFR Mumbai was supported by the Department of Atomic Energy of the Government of India under project number 12-R&D-TFR-5.10-0100.

* These authors contributed equally to this work
† bahadur.singh@tifr.res.in
‡ jsun@tulane.edu

[1] P. Coleman, *Heavy Fermions: Electrons at the Edge of Magnetism*, Vol. 38 (Wiley, 2007) pp. 95–148.
[2] S. Kirchner, S. Paschen, Q. Chen, S. Wirth, D. Feng, J. D. Thompson, and Q. Si, Rev. Mod. Phys. **92**, 011002 (2020).
[3] S. Paschen and Q. Si, Nat. Rev. Phys. **3**, 9 (2021).
[4] V. Ivanov, X. Wan, and S. Y. Savrasov, Phys. Rev. X **9**, 041055 (2019).
[5] Y. Shao, A. N. Rudenko, J. Hu, Z. Sun, Y. Zhu, S. Moon, A. J. Millis, S. Yuan, A. I. Lichtenstein, D. Smirnov, Z. Q. Mao, M. I. Katsnelson, and D. N. Basov, Nat. Phys. **16**, 636 (2020).
[6] H.-H. Lai, S. E. Grefe, S. Paschen, and Q. Si, Proc. Natl. Acad. Sci. **115**, 93 (2018).
[7] C. Cao, G.-X. Zhi, and J.-X. Zhu, Phys. Rev. Lett. **124**, 166403 (2020).
[8] R. Zhang, B. Singh, C. Lane, J. Kidd, Y. Zhang, B. Barbiellini, R. S. Markiewicz, A. Bansil, and J. Sun, arXiv e-prints , arXiv:2003.11052 (2020), arXiv:2003.11052 [cond-mat.str-el].
[9] H. Pirie, Y. Liu, A. Soumyanarayanan, P. Chen, Y. He, M. M. Yee, P. F. S. Rosa, J. D. Thompson, D.-J. Kim, Z. Fisk, X. Wang, J. Paglione, D. K. Morr, M. H. Hamidian, and J. E. Hoffman, Nat. Phys. **16**, 52 (2020).
[10] L. Li, K. Sun, C. Kurdak, and J. W. Allen, Nat. Rev. Phys. **2**, 463 (2020).
[11] P.-Y. Chang, O. Erten, and P. Coleman, Nat. Phys. **13**, 794 (2017).
[12] H.-Y. Yang, B. Singh, J. Gaudet, B. Lu, C.-Y. Huang, W.-C. Chiu, S.-M. Huang, B. Wang, F. Bahrami, B. Xu,

J. Franklin, I. Sochnikov, D. E. Graf, G. Xu, Y. Zhao, C. M. Hoffman, H. Lin, D. H. Torchinsky, C. L. Broholm, A. Bansil, and F. Tafti, Phys. Rev. B **103**, 115143 (2021).
[13] G. Chang, B. Singh, S.-Y. Xu, G. Bian, S.-M. Huang, C.-H. Hsu, I. Belopolski, N. Alidoust, D. S. Sanchez, H. Zheng, H. Lu, X. Zhang, Y. Bian, T.-R. Chang, H.-T. Jeng, A. Bansil, H. Hsu, S. Jia, T. Neupert, H. Lin, and M. Z. Hasan, Phys. Rev. B **97**, 041104 (2018).
[14] H.-Y. Yang, B. Singh, B. Lu, C.-Y. Huang, F. Bahrami, W.-C. Chiu, D. Graf, S.-M. Huang, B. Wang, H. Lin, D. Torchinsky, A. Bansil, and F. Tafti, APL Mater. **8**, 011111 (2020).
[15] M. Dzero, J. Xia, V. Galitski, and P. Coleman, Annu. Rev. Condens. Matter Phys. **7**, 249 (2016).
[16] D. S. Sanchez, G. Chang, I. Belopolski, H. Lu, J.-X. Yin, N. Alidoust, X. Xu, T. A. Cochran, X. Zhang, Y. Bian, S. S. Zhang, Y.-Y. Liu, J. Ma, G. Bian, H. Lin, S.-Y. Xu, S. Jia, and M. Z. Hasan, Nat. Commun. **11**, 3356 (2020).
[17] S. Nie, Y. Sun, F. B. Prinz, Z. Wang, H. Weng, Z. Fang, and X. Dai, Phys. Rev. Lett. **124**, 076403 (2020).
[18] S.-Y. Gao, S. Xu, H. Li, C.-J. Yi, S.-M. Nie, Z.-C. Rao, H. Wang, Q.-X. Hu, X.-Z. Chen, W.-H. Fan, J.-R. Huang, Y.-B. Huang, N. Pryds, M. Shi, Z.-J. Wang, Y.-G. Shi, T.-L. Xia, T. Qian, and H. Ding, Phys. Rev. X **11**, 021016 (2021).
[19] J. Effantin, J. Rossat-Mignod, P. Burlet, H. Bartholin, S. Kunii, and T. Kasuya, J. Magn. Magn. Mater. **47-48**, 145 (1985).
[20] P. Y. Portnichenko, A. Akbari, S. E. Nikitin, A. S. Cameron, A. V. Dukhnenko, V. B. Filipov, N. Y. Shitsevalova, P. Čermák, I. Radelytskyi, A. Schneidewind, J. Ollivier, A. Podlesnyak, Z. Huesges, J. Xu, A. Ivanov, Y. Sidis, S. Petit, J.-M. Mignot, P. Thalmeier, and D. S. Inosov, Phys. Rev. X **10**, 021010 (2020).
[21] M. Ye, H. H. Kung, P. F. Rosa, E. D. Bauer, Z. Fisk, and G. Blumberg, Phy. Rev. Mater. **3**, 1 (2019).
[22] O. Zaharko, P. Fischer, A. Schenck, S. Kunii, P.-J. Brown, F. Tasset, and T. Hansen, Phys. Rev. B **68**, 214401 (2003).
[23] E. Liu, Y. Sun, N. Kumar, L. Muechler, A. Sun, L. Jiao, S.-Y. Yang, D. Liu, A. Liang, Q. Xu, J. Kroder, V. Süß, H. Borrmann, C. Shekhar, Z. Wang, C. Xi, W. Wang, W. Schnelle, S. Wirth, Y. Chen, S. T. B. Goennenwein, and C. Felser, Nat. Phys. **14**, 1125 (2018).
[24] H. Gao, J. W. Venderbos, Y. Kim, and A. M. Rappe, Annu. Rev. Mater. Res. **49**, 153 (2019).
[25] H. Weng, C. Fang, Z. Fang, B. A. Bernevig, and X. Dai, Phys. Rev. X **5**, 011029 (2015).
[26] T.-R. Chang, I. Pletikosic, T. Kong, G. Bian, A. Huang, J. Denlinger, S. K. Kushwaha, B. Sinkovic, H.-T. Jeng, T. Valla, W. Xie, and R. J. Cava, Adv. Sci. **6**, 1800897 (2019).
[27] B.-B. Fu, C.-J. Yi, T.-T. Zhang, M. Caputo, J.-Z. Ma, X. Gao, B. Q. Lv, L.-Y. Kong, Y.-B. Huang, P. Richard, M. Shi, V. N. Strocov, C. Fang, H.-M. Weng, Y.-G. Shi, T. Qian, and H. Ding, Sci. Adv. **5**, eaau6459 (2019).
[28] G. Chang, S.-Y. Xu, X. Zhou, S.-M. Huang, B. Singh, B. Wang, I. Belopolski, J. Yin, S. Zhang, A. Bansil, H. Lin, and M. Z. Hasan, Phys. Rev. Lett. **119**, 156401 (2017).
[29] B. Bradlyn, J. Cano, Z. Wang, M. G. Vergniory, C. Felser, R. J. Cava, and B. A. Bernevig, Science **353**, aaf5037 (2016).
[30] S. Mardanya, B. Singh, S.-M. Huang, T.-R. Chang, C. Su, H. Lin, A. Agarwal, and A. Bansil, Phys. Rev. Mater. **3**, 071201 (2019).
[31] B. Singh, G. Chang, T.-R. Chang, S.-M. Huang, C. Su, M.-C. Lin, H. Lin, and A. Bansil, Sci. Rep. **8**, 10540 (2018).
[32] S.-M. Huang, S.-Y. Xu, I. Belopolski, C.-C. Lee, G. Chang, T.-R. Chang, B. Wang, N. Alidoust, G. Bian, M. Neupane, D. Sanchez, H. Zheng, H.-T. Jeng, A. Bansil, T. Neupert, H. Lin, and M. Z. Hasan, Proc. Natl. Acad. Sci. **113**, 1180 (2016).
[33] I. Belopolski, K. Manna, D. S. Sanchez, G. Chang, B. Ernst, J. Yin, S. S. Zhang, T. Cochran, N. Shumiya, H. Zheng, B. Singh, G. Bian, D. Multer, M. Litskevich, X. Zhou, S.-M. Huang, B. Wang, T.-R. Chang, S.-Y. Xu, A. Bansil, C. Felser, H. Lin, and M. Z. Hasan, Science **365**, 1278 (2019).
[34] H. Jang, G. Friemel, J. Ollivier, A. V. Dukhnenko, N. Y. Shitsevalova, V. B. Filipov, B. Keimer, and D. S. Inosov, Nat. Mater. **13**, 682 (2014).
[35] G. Kresse and J. Hafner, Phys. Rev. B **48**, 13115 (1993).
[36] G. Kresse and J. Furthmüller, Phys. Rev. B **54**, 11169 (1996).
[37] G. Kresse and D. Joubert, Phys. Rev. B **59**, 1758 (1999).
[38] J. Sun, A. Ruzsinszky, and J. Perdew, Phys. Rev. Lett. **115**, 036402 (2015).
[39] Y. Zhang, C. Lane, J. W. Furness, B. Barbiellini, J. P. Perdew, R. S. Markiewicz, A. Bansil, and J. Sun, Proc. Natl. Acad. Sci. **117**, 68 (2020).
[40] J. W. Furness, Y. Zhang, C. Lane, I. G. Buda, B. Barbiellini, R. S. Markiewicz, A. Bansil, and J. Sun, Commun. Phys. **1**, 11 (2018).
[41] C. Lane, J. W. Furness, I. G. Buda, Y. Zhang, R. S. Markiewicz, B. Barbiellini, J. Sun, and A. Bansil, Phys. Rev. B **98**, 125140 (2018).
[42] R. Zhang, C. Lane, B. Singh, J. Nokelainen, B. Barbiellini, R. S. Markiewicz, A. Bansil, and J. Sun, Commun. Phys. **4**, 118 (2021).
[43] Y. Zhang, J. Furness, R. Zhang, Z. Wang, A. Zunger, and J. Sun, Phys. Rev. B **102**, 045112 (2020).
[44] G. Pizzi, V. Vitale, R. Arita, S. Blgel, F. Freimuth, G. Géranton, M. Gibertini, D. Gresch, C. Johnson, T. Koretsune, J. Ibañez-Azpiroz, H. Lee, J.-M. Lihm, D. Marchand, A. Marrazzo, Y. Mokrousov, J. I. Mustafa, Y. Nohara, Y. Nomura, L. Paulatto, S. Poncé, T. Ponweiser, J. Qiao, F. Thle, S. S. Tsirkin, M. Wierzbowska, N. Marzari, D. Vanderbilt, I. Souza, A. A. Mostofi, and J. R. Yates, J. Phys. Condens. Matter **32**, 165902 (2020).
[45] F. Guinea, C. Tejedor, F. Flores, and E. Louis, Phys. Rev. B **28**, 4397 (1983).
[46] M. L. Sancho, J. L. Sancho, and J. Rubio, J. Phys. F: Met. Phys **14**, 1205 (1984).
[47] N. Foroozani, J. Lim, G. Fabbris, P. Rosa, Z. Fisk, and J. Schilling, Physica B Condens. Matter **457**, 12 (2015).
[48] See Supplemental Material at [URL will be inserted by publisher] for total energies of CeB_6 with various magnetic phase, band structures with variable spin-orbit coupling, energy dispersion of pseudo-nodal surface, locations of Weyl points, and topological surface states for CeB_6.
[49] Z. Wang, X.-G. Zhao, R. Koch, S. J. L. Billinge, and A. Zunger, Phys. Rev. B **102**, 235121 (2020).
[50] A. V. Semeno, S. Okubo, H. Ohta, and S. V. Demishev, Appl. Magn. Reson. **52**, 459 (2021).

[51] C. K. Barman, P. Singh, D. D. Johnson, and A. Alam, Phys. Rev. Lett. **122**, 076401 (2019).
[52] H. Lu and L. Huang, Phys. Rev. B **95**, 155140 (2017).
[53] M. Neupane, N. Alidoust, I. Belopolski, G. Bian, S. Y. Xu, D. J. Kim, P. P. Shibayev, D. S. Sanchez, H. Zheng, T. R. Chang, H. T. Jeng, P. S. Riseborough, H. Lin, A. Bansil, T. Durakiewicz, Z. Fisk, and M. Z. Hasan, Phys. Rev. B **92**, 2 (2015).
[54] A. Koitzsch, N. Heming, M. Knupfer, B. Büchner, P. Y. Portnichenko, A. V. Dukhnenko, N. Y. Shitsevalova, V. B. Filipov, L. L. Lev, V. N. Strocov, J. Ollivier, and D. S. Inosov, Nat. Commun. **7**, 1 (2016).
[55] J. Wang, Y. Liu, K.-H. Jin, X. Sui, L. Zhang, W. Duan, F. Liu, and B. Huang, Phys. Rev. B **98**, 201112(R) (2018).
[56] O. b. u. Türker and S. Moroz, Phys. Rev. B **97**, 075120 (2018).
[57] C. Fang, M. J. Gilbert, X. Dai, and B. A. Bernevig, Phys. Rev. Lett. **108**, 266802 (2012).
[58] B. A. Bernevig, *Topological insulators and topological superconductors* (Princeton university press, 2013).